Versatile Design of Functional Organic–Inorganic 3D-Printed (Opto)Electronic Interfaces with Custom Catalytic Activity

Jose Muñoz,[a] Edurne Redondo,[a] Martin Pumera[a,b,c,d,*]

[a]Future Energy and Innovation Laboratory, Central European Institute of Technology, Brno University of Technology (CEITEC-BUT), Purkyňova 123, 61200 Brno, Czech Republic

[b]Department of Chemistry and Biochemistry, Mendel University in Brno, Zemedelska 1/1665, 613 00 Brno, Czech Republic

[c]Department of Chemical and Biomolecular Engineering, Yonsei University, 50 Yonsei-ro, Seodaemun-Gu, Seoul 03722, South Korea

[d]Department of Medical Research, China Medical University Hospital, China Medical University, No. 91 Hsueh-Shih Road, Taichung 40402, Taiwan

Abstract

The ability to combine organic and inorganic components in a single material represents a great step towards the development of advanced (opto)electronic systems. Nowadays, 3D printing technology has generated a revolution in the rapid prototyping and low-cost fabrication of 3D-printed electronic devices. However, a main drawback when using 3D-printed transducers is the lack of robust functionalization methods for tuning their capabilities. Herein, we report *in situ* functionalization approach to tailor the capabilities of 3D printed structures with functional inorganic nanoparticles (FINPs), which are appealing active units for electronic, optical and catalytic applications. We present a simple, general and robust immobilization method of a battery of FINPs (*i.e.*, metal nanoparticles and quantum dots) upon 3D-printed nanocomposite carbon/polymer electrode (3D-nCE) surfaces. The versatility of the resulting functional organic–inorganic 3D-printed electronic interfaces has been provided in different pivotal areas of electrochemistry, including *i)* electrocatalysis, *ii)* bio-electroanalysis, *iii)* energy (storage and conversion) and *iv)* photoelectrochemical applications. Overall, the synergism of combining the transducing characteristics of 3D-nCEs with the implanted tuning surface capabilities of FINPs leads to new/enhanced electrochemical performances when compared to their bare 3D-nCE counterparts. Accordingly, this work elucidates that FINPs have much to offer in the field of 3D-printing technology and provides the bases towards the green fabrication of functional organic–inorganic 3D-printed (opto)electronic interfaces with custom catalytic activity.

Keywords: 3D-Printed Electrodes, Metal Nanoparticles, Quantum Dots, Surface Engineering, Electrocatalysis

1. Introduction

Surface engineering has been responsible to light up different nanocomposites made of both inorganic and organic components for their custom application in extremely divers fields.[1],[2],[3],[4],[5] Particularly, the use of functional inorganic nanoparticles (FINPs) has received considerable attention owing to their catalytic and electrochemical features, providing great benefits for the development of advanced electrochemical transducers (electrodes).[6],[7],[8],[9],[10],[11] FINPs, such as metal nanoparticles (MNPs) and quantum dots (QDs), are nanostructural elements which can exhibit unique properties and functions due to their electronic and optical properties.[12],[13],[14],[15] This has led to functionalize different types of conductive materials with FINPs acting as transducing platforms, achieving amplified electrochemical signals through a finely divided and enlarged interface formation. Further, the catalytic characteristics of FINPs can be modulated by simply manipulating the synthetic conditions.[16],[17],[18] Among the several ways to tune electrodes with FINPs, the intermatrix synthesis (IMS) technique has proven to be a straightforward green strategy for the *in situ* incorporation of several

FINPs upon different carbon-rich substrates (e.g., carbon nanotubes, graphene, nanodiamonds, etc.).[19],[20]

In this new era of nanotechnology —also so-called as "Fourth Industrial Revolution"—, 3D printing technology is being at the forefront of electronic devices research since it allows the large-scale and cost-effective prototyping of extremely customizable designs in a matter of minutes.[21],[22],[23],[24],[25] Concretely, fused deposition modeling (FDM) is one of the most employed 3D printing strategies for electrodes development due to the current availability of conductive carbon-based nanocomposite filaments.[26],[27] Nowadays, 3D-printed nanocomposite carbon electrodes (3D-nCEs) made of graphene and polylactic acid (PLA) are being extensively used for several electrochemical applications, including electroanalysis,[28],[29],[30],[31] energy (storage and conversion)[32],[33],[34],[35] and switching memories.[36] However, a main limitation when using 3D-nCEs can be clearly identified: the lack of effective (bio)functionalization methods for tuning their functional capabilities, being mainly limited to the use of weak physisorption or costly sputtering processes.[31] Although, the inherent inorganic impurities on 3D-nCEs have recently exhibited catalytic activity for energy approaches,[37],[38] the functionalization of 3D-nCEs with FINPs to achieve functional inorganic–organic 3D-printed interfaces for electrocatalytic approaches is nowadays an unexplored field.

Herein, motivated by the possibility to overcome the current bottleneck involving 3D-printed electronic devices, the preparation and catalytic applications of FINPs supported on 3D-nCEs is provided. For this aim, a simple bottom-up functionalization approach has been devised for the general design of functional organic–inorganic 3D-printed electronic interfaces as unconventional catalytic systems (see **Scheme 1**). The carbon reactivity of 3D-nCE substrates has been exploited for anchoring a battery of

FINPs (*i.e.*, Ag–, Au–, Cu–, Pd– and Pt–MNPs, and CdS–QDs) *via* IMS technique, resulting in FINPs@3D-nCE devices. Interestingly, the versatility of the transferred electrical, optical and catalytic properties from the FINPs to the carbon-based 3D-printed transducers has been demonstrated in pivotal areas of electrochemistry, including *i)* electrocatalysis, *ii)* bio-sensing, *iii)* energy (storage and conversion) and *iv)* photoelectrochemical applications. Accordingly, this approach opens up new avenues towards the custom development of the next generation of functional organic–inorganic 3D-printed materials acting as highly-efficient catalytic platforms.

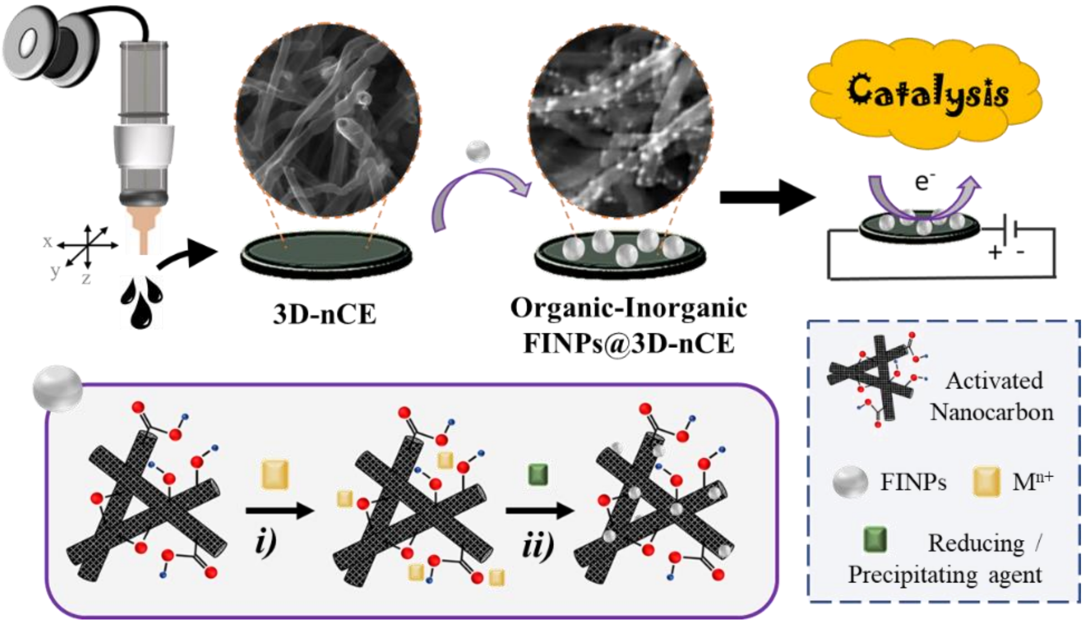

Scheme 1. Illustration approach for the development of functional organic–inorganic 3D-printed electronic devices acting as catalytic interfaces. 3D printing is used for manufacturing 3D-nCE, which are functionalized with a wide range of FINPs *via* IMS. Inset: Two sequential stages for FINPs incorporation: *i)* electrostatic M^{n+} loading upon the activated nanocarbon and *ii)* subsequent FINPs crystallization through the addition of either a reducing ($NaBH_4$) or precipitating (S^{2-}) agent for MNPs and QDs, respectively.

2. Results and Discussion

2.1. Synthesis of FINPs@3D-nCEs via IMS

3D-nCEs were printed by FDM using a commercially available graphene/PLA filament (see Supporting Information for experimental details). In order to achieve electrically active substrates, as-printed 3D-nCEs were chemically (solvent: DMF; time: 3h) and electrochemically (bias potential: 2.5 V; time: 300 s; electrolyte: 0.1 M phosphate buffer solution, PBS) activated following the standard protocol.[39],[40] Afterwards, the activated electrodes were *in situ* functionalized with a battery of FINPs —*i.e.*, Ag, Au, Cu, Pd and Pt metal nanoparticles (MNPs) and CdS quantum dots (QDs)— *via* IMS. IMS relies on an eco-friendly technology that allows the covalent functionalization of active carbon surfaces with different metal ions by taking advantage of the ion-exchange capabilities of the support.[19] The driving force of this approach is based on the electrostatic interactions between the M^{n+} precursor and the oxygenated groups from the activated graphene exposed on the 3D-nCE surface prior to reduction/precipitation. Thus, six different FINPs@3D-nCEs were fabricated by following two sequential steps (see **Scheme 1** for illustration):

i) Electrostatic loading of metal ions (M^{n+}): Activated 3D-nCEs were immersed in a 2.5 mM aqueous solution of the M^{n+} precursor —where M^{n+} is Ag^{+}, Au^{3+}, Cu^{2+}, Pd^{2+} Pt^{2+} or Cd^{2+}— for 1 h, fact that promotes electrostatic interactions between the oxygenated groups exposed on the graphene walls and the M^{n+} precursor.

ii) Crystallization of the FINPs: Subsequently, the loaded 3D-nCEs were transferred to a 10 mM reducing/precipitating agent solution ($NaBH_4$ or NaHS for MNPs and QDs, respectively) for 15 min to induce the crystallization of the FINPs on the top of the carbon support.

2.2. Characterization of FINPs@3D-nCEs:

The resulting organic–inorganic FINPs@3D-nCE devices were characterized by means of scanning electron microscopy (SEM), X-ray photoelectron spectroscopy (XPS), Raman and electrochemical impedance spectroscopy (EIS). In all cases, the activated 3D-nCE (prior to functionalization) was also studied for comparison.

On one hand, the five developed MNPs@3D-nCE devices (a) before and after being functionalized with (b) Ag–MNPs, (c) Au–MNPs, (d) Cu–MNPs, (e) Pd–MNPs and (f) Pt–MNPs were analyzed. Firstly, the morphological characteristics of the organic–inorganic 3D-printed electrode surfaces were studied by means of SEM (**Figure 1**). A homogeneous carbon walls functionalization with MNPs was clearly achieved when compared with the non-modified 3D-nCE surface, suggesting that 3D-nCEs were successfully decorated by a large quantity of MNPs *via* IMS. In general, the IMS approach led to the formation of spherical MNPs except for Cu–MNPs, which could be related to the oxidation of Cu–MNPs in air (see **Figure S1**, high-resolution XPS spectra of Cu 2p).[41]

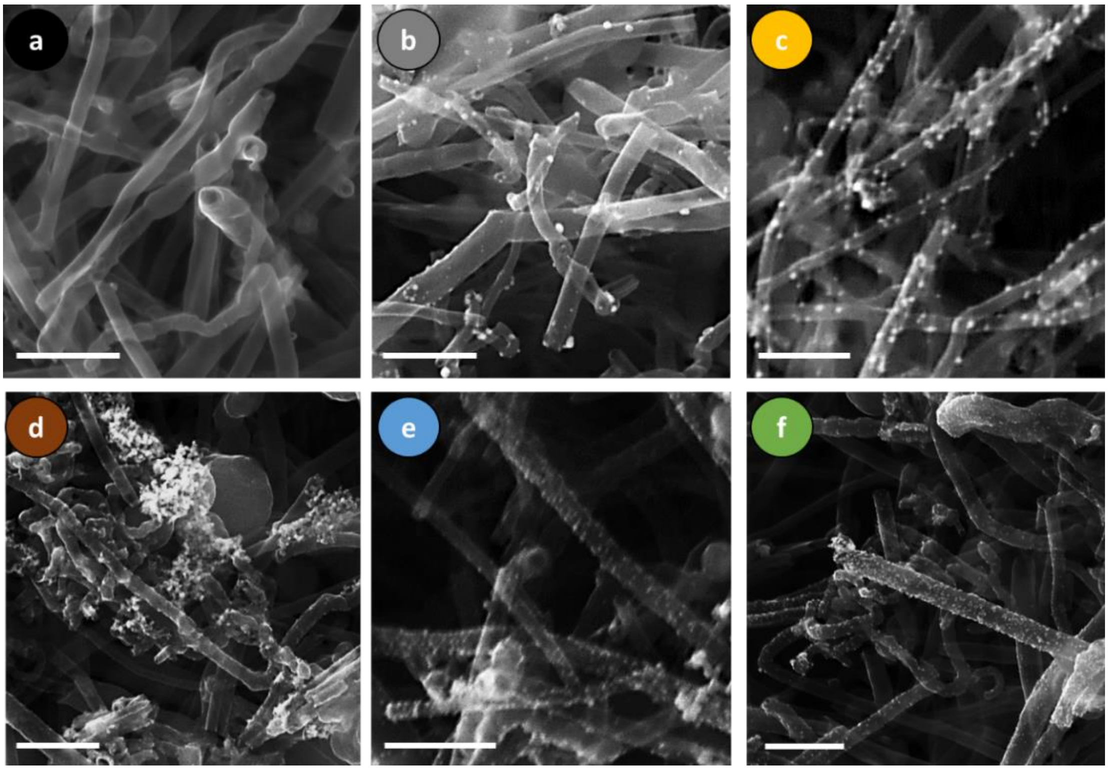

Figure 1. Morphological characterization of MNPs@3D-nCEs. SEM images of unmodified 3D-nCE (a) and MNPs@3D-nCEs: (b) Ag@3D-nCE, (c) Au@3D-nCE, (d) Cu@3D-nCE, (e) Pd@3D-nCE and (f) Pt@3D-nCE. Scale bar: 500 nm.

Further characterization of MNPs@3D-nCEs was characterized by means of XPS. As expected, the wide-range survey XPS spectra from **Figure 2A** displayed C 1s and O 1s as the two major elements in all samples because of the graphene/PLA nature of 3D-nCEs (spectrum a). Importantly, additional peaks after *in situ* MNPs immobilization were clearly observed, which corresponds to b) Ag 3d, c) Au 4f and 4d, d) Cu 2p, e) Pd 3d and f) Pt 4f main peaks. The quantification of MNPs on the 3D-nCE surface was estimated to be between 1.8% (Cu@3D-nCE) and 9.2% (Ag@3D-nCE). Additionally, Raman spectra from **Figure 2B** presents two well defined bands located at around 1350 and 1580 cm^{-1} corresponding to the topological defects (D band) and the crystalline graphitic regions (G band) from the graphene filler, respectively.[42] After 3D-nCE functionalization with MNPs, the intensity ratio of the D and G bands (I_D/I_G) of the non-functionalized electrode (0.89) significantly decreased, indicating a lower level of disorder in the carbon material. Such phenomena can be ascribed to the exposure of electrodes to a reducing agent solution ($NaBH_4$) for MNPs crystallization, which is known to promote the reduction of the graphene filler.[43],[44] Therefore, these characterization results clearly confirmed the incorporation of several MNPs upon 3D-nCE substrates *via* IMS.

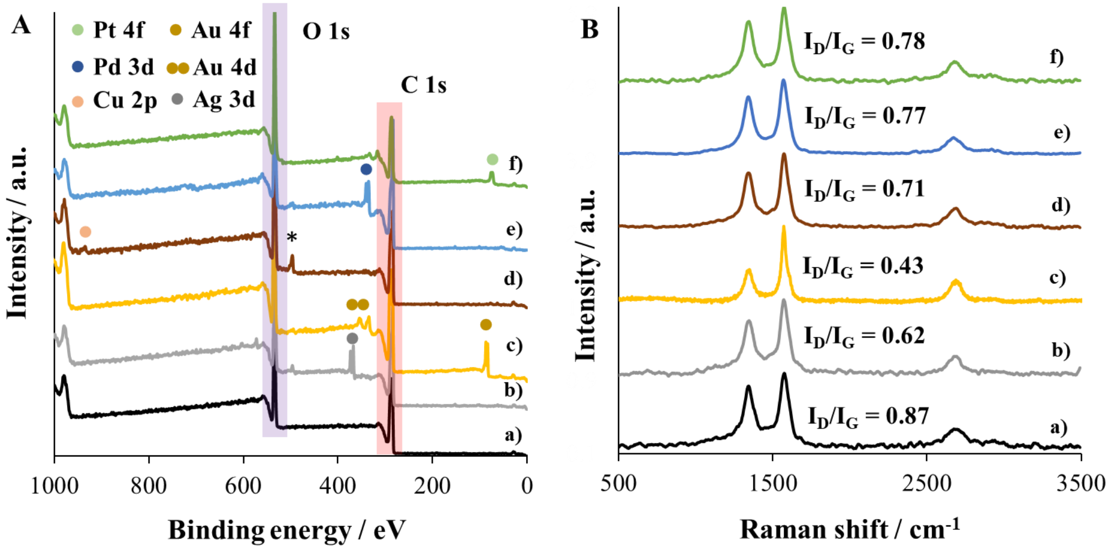

Figure 2. Spectroscopic characterization of MNPs@3D-nCEs. A) Wide-range survey XPS spectra and B) Raman spectra of unmodified 3D-nCE (a) and functionalized MNPs@3D-nCEs: (b) Ag@3D-nCE, (c) Au@3D-nCE, (d) Cu@3D-nCE, (e) Pd@3D-nCE and (f) Pt@3D-nCE. (*) Ti 2p peak corresponding to the inherent metallic impurities present in the raw graphene/PLA filament.[37],[38]

On the other hand, **Figure 3** shows same characterization studies carried out at the 3D-nCEs functionalized with CdS–QDs (CdS@3D-nCE). As shown in **Figure 3A**, CdS–QDs were quite difficult to be visualized by SEM due to their small size (IMS is known to provide CdS–QDs with sizes around 2 nm).[19] However, its XPS wide scan spectrum (**Figure 3B**) clearly confirmed the incorporation of CdS–QDs on 3D-nCE surfaces through the presence of both S 2p and Cd 3d peaks. Importantly, XPS deconvolutions (**Figure 3B**, inset) presented the general CdS–QDs contributions: Cd $3d_{3/2}$ and Cd $3d_{5/2}$ contributions at 411.8 and 405 eV from Cd^{2+} and S $2p_{3/2}$ and S $2p_{1/2}$ contributions at 162.2 and 161.3 eV from S^{2-}, respectively.[45] In addition, Raman spectrum also confirmed a notable I_D/I_G decreased from 0.89 to 0.63 after CdS–QDs functionalization, indicating a lower defect density of CdS@3D-nCEs as compared to non-modified 3D-nCEs. These results confirm a proper functionalization of 3D-nCEs with CdS–QDs.

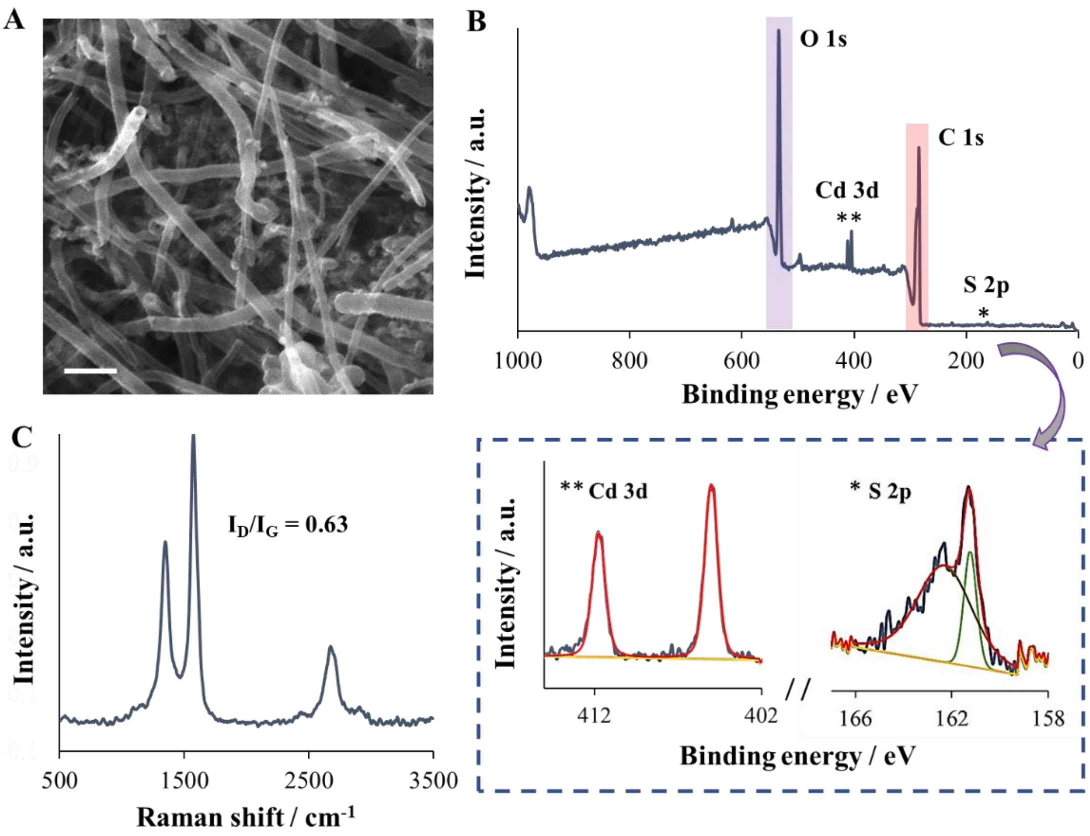

Figure 3. Physical characterization of CdS@3D-nCEs. A) Morphological SEM images (scale bar: 500 nm). B) XPS wide scan spectrum (inset: S 2p and Cd 3d deconvolutions and C) its corresponding Raman spectrum.

Finally, the electrochemical characteristics of the developed organic–inorganic FINPs@3D-nCEs were explored by means of EIS. **Figure S2** presents the Bode magnitude plot (impedance modulus, |Z| *vs.* frequency, *f*) from EIS recorded in a 10 mM $[Fe(CN)_6]^{3-/4-}$ redox marker solution containing 0.1 M KCl. In all cases, a remarkable |Z| decrease after functionalizing 3D-nCEs with FINPs incorporation was observed, fact that guarantees hybrid organic–inorganic 3D-printed electrodes with fast electron transfer.[20] Such phenomena can be ascribed to the intrinsic high surface-to-volume ratio as well as rich active surface atoms of FINPs that provides transducers with higher electroactive area as compared with their pristine counterparts.[46] This demonstrates the key role of FINPs to enhance the interfacial electron transfer process at the 3D-printed electrochemical transducer by transferring their catalytic properties, leading to the achievement of organic–inorganic FINPs@3D-nCEs exhibiting improved electrochemical capabilities.

According to these characterization results, IMS has proven to be a powerful and versatile strategy for the *in situ* functionalization of 3D-printed electronic devices with different types of FINPs, such as Ag–MNPs, Au–MNPs, Cu–MNPs, Pd–MNPs, and Pt–MNPs as well as CdS–QDs.

2.2. Electrochemical achievements of functional organic–inorganic 3D-printed electronic interfaces

Having verified the excellent electrochemical performances of the developed FINPs@3D-nCEs —and taking into account the inherent electrical/optical catalytic capabilities of each FINP—, the next step was focused on interrogating the benefits of functionalizing 3D-nCEs with FINPs in different areas of electrochemistry. For this goal, each functional organic–inorganic 3D-printed electronic interface was explored for a task-specific electrochemical application in the field of *i)* electrocatalysis (Pt@3D-nCE), *ii)* bio-electroanalysis (Ag@3D-nCE and Au@3D-nCE), *iii)* energy storage (Cu@3D-nCE) and conversion (Pd@3D-nCE), and *iv)* photoelectrochemistry (CdS@3D-nCE). For comparison, control experiments were run by employing the unmodified 3D-nCE. For electrochemical measurements, the different 3D-printed electrodes were used as working electrodes in a three-electrode configuration cell filled with the corresponding electrolyte, where an Ag/AgCl and a Pt wire were utilized as reference and counter electrodes, respectively (see **Figure S3** and the Experimental Section from Supporting Information for more experimental details).

2.2.1. Electrocatalysis

The incorporation of MNPs upon electrochemical transducers is particularly appealing since they can provide several catalytic benefits. In this regard, the electrocatalytic capabilities of Pt–MNPs were explored to pursue high surface-area 3D-printed electrodes, fact that is known to decrease overpotentials. For this aim, H_2O_2 was utilized as a model redox-active analyte. From an electrochemical point of view, the determination of reactive oxygen species at low potentials (*i.e.* oxidation of H_2O_2 to H_2O and O_2 catalyzed by Pt) is extremely important since many biological reactions involving complex matrices generate H_2O_2 as by-product.[47] Further, the decomposition of H_2O_2 catalyzed by Pt is also important for energy conversion applications.[48] **Figure 4** show the lineal sweep voltammograms (LSV) at the (a) unmodified 3D-nCE and (b) Pt@3D-nCEs towards the determination of H_2O_2. Remarkably, the electrocatalytic activity of Pt–MNPs yielded to an overpotential decrease from 0.86 V to 0.45 V, which supposes a remarkable 48% improvement. Further, the electrode sensitivity was also enhanced after Pt–MNPs incorporation. Thus, while the unmodified 3D-nCE did not present a lineal trend with increasing the [H_2O_2], the hybrid Pt@3D-nCE exhibited an excellent lineal regression ($r^2 = 0.992$) in the range of 0.1 to 1.0 μM (see **Figure 4b)**, inset). Accordingly, the electrocatalytic activity of Pt–MNPs upon 3D-nCEs is demonstrated since they not only decreased overpotentials but also enhanced the sensitivity of the 3D-printed electronic device.

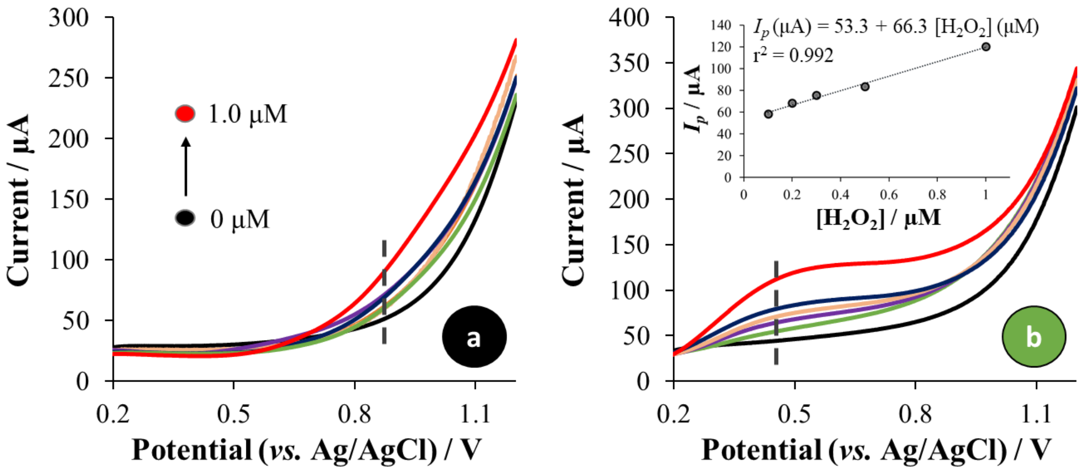

Figure 4. Electrocatalytic capabilities of organic–inorganic 3D-printed electronic interfaces. LSV at the (a) unmodified 3D-nCE and (b) Pt@3D-nCE towards the determination of different concentrations (0.1, 0.2, 0.3, 0.5, and 1 µM) of H_2O_2 with its corresponding calibration curve (inset). Experimental conditions: electrolyte: PBS at pH 7.2; scan rate: 50 mV·s^{-1}.

2.2.2. Bio-electroanalysis

The use of MNPs for the development of electrochemical biosensing devices is a valuable strategy to promote local microenvironments that can lead to specific and selective interactions with substrates.[13] Herein, the benefits of functionalizing 3D-nCEs with Ag–MNPs and Au–MNPs for bio-electroanalysis approaches have been interrogated (**Figure 5**).

Firstly, Ag@3D-nCEs were used to selectively promote redox interactions with a specific target to enhance sensitivity and detection limits. As a proof, glucose oxidase (GOx) was physically immobilized on the Ag@3D-nCE surface (GOx/Ag@3D-nCE) for the indirect determination of glucose (see Supporting Information for experimental details). Although the catalytic activity of Ag–MNPs has already shown to enhance sensitivities in glucose biosensors,[49] the electroanalytical assay employed here novelty relies on voltammetrically monitoring changes at the Ag/Ag$^+$ intensity peak found at 0.24 V (*vs.* Ag/AgCl). The reactivity between Ag–MNPs and the H_2O_2 by-product produced from the GOx/glucose enzymatic system allowed the indirect quantification of glucose by taking advantage of the following reaction: $Ag + H_2O_2 \rightarrow Ag^+ + 2\ OH^-$.[50] As shown in **Figure 5a**, an anodic peak decrease with increasing the concentration of glucose was observed since the more H_2O_2 is produced, the more Ag–MNPs are consumed. The calibration curve from **Figure 5a** (inset) displayed the following regression equation for the GOx/Ag@3D-nCE: I_p (μA) = 110.6 – 34.46 log [Glucose] (mM), with $r^2 = 0.99$, demonstrating that the biosensor is capable to determine glucose in the range of 0.91 to 3.3 mM. Additionally, the non-responsive electrochemical behavior of the GOx/3D-nCE biosensor with increasing [glucose] (**Figure S4**, control experiment) clearly verify the key role of Ag–MNPs for indirectly monitoring glucose.

Otherwise, Au–MNPs were exploited as useful nanotemplates for the assembly of supramolecular moieties acting as highly-sensitive biorecognition systems *via* gold-thiol interactions.[51] Concretely, Au@3D-nCEs were biofunctionalized with a thiolated β-cyclodextrin (β–CD/Au@3D-nCE, see Supporting Information for experimental details), a macrocycle capable to selectively host different target enantiomers (*i.e.*, amino acids).[52] Thus, the resulting β–CD/Au@3D-nCE was exploited towards the voltammetric enantiodiscrimination of tryptophan (Trp) enantiomers *via* supramolecular host-guest interactions. As shown in **Figure 5b**, the favorable chiral environment promoted by the inclusion complex generation between Trp enantiomers and β–CD/Au@3D-nCE allowed an excellent electrochemical discrimination of Trp enantiomers at the β–CD/Au@3D-nCE. An excellent selectivity for L–Trp with an enantioselectivity coefficient of 1.89 over D–Trp —estimated by means of peak current ratio, I_L/I_D— was achieved, also pointing out a notable peak-to-peak separation (ΔE_{L-D}) value of 60 mV. Such an enantioselectivity is in agreement with other CD-based electrodes reported for Trp enantiomers. Importantly, a control experiment was carried out at the Au@3D-nCE. As shown in **Figure S5**, the almost overlapped voltammograms (I_L/I_D of 0.99 and ΔE_{L-D} of 0 mV) clearly indicates that the Au@3D-nCE cannot discriminate between Trp enantiomers due to the absence of the chiral moiety (β–CD). This verifies the suitability of Au–MNPs to further functionalize 3D-nCEs with recognition elements for biosensing approaches. It is important to highlight that, to the best of our knowledge, it is the first time that the intrinsic chirality of β–CD is explored on 3D-printed devices for electroanalysis.

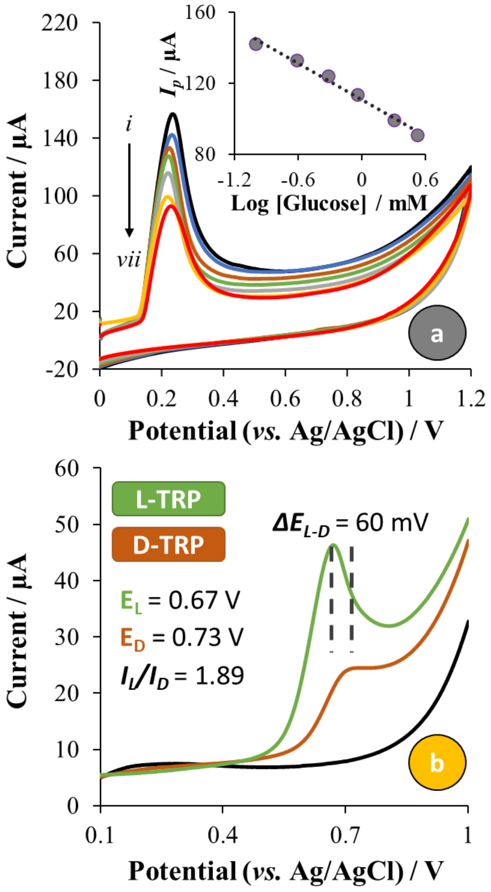

Figure 5. Organic–inorganic 3D-printed electronic interfaces for bio-electroanalytical approaches. (a) Cyclic voltammograms run at the GOx/Ag@3D-nCE before and after adding different [glucose]: *i)* 0, *ii)* 0.10, *iii)* 0.24, *iv)* 0.48, *v)* 0.91, *vi)* 2.0 and *vii)* 3.3 mM. Glucose was indirectly determined by monitoring the intensity peak decrease at the Ag/Ag$^+$ redox peak. Inset: Calibration plot. (b) LSV performance at the β–CD/Au@3D-nCE before (dash line) and after adding a fixed concentration of the chiral targets (L–Trp and D–Trp). Electrochemical experiments were carried out in PBS at pH 7.2 (scan rate: 50 mV·s^{-1}).

2.2.3. Energy storage and conversion

3D-printed electrochemical energy systems have gained great attention due to the great manufacturing control over the thickness and shape of the electrodes that 3D printing technology enables.[22] Thus, MNPs have been also explored as inorganic catalytic mediators for the design of 3D-printed electrochemical energy systems, a challenging field towards the eco-friendly development of alternative CO_2-free fuels or energy storage technologies as contenders to petroleum-based sources.

Regarding energy conversion, the hydrogen evolution reaction (HER) involves the electrochemical water splitting for H_2 production *via* a two-electron transfer reaction, following the formula: $2\ H^+ + 2e^- \rightarrow H_2$. Commonly, Pt group metals are utilized as electrocatalysts for HER since they exhibit low overpotentials for H_2 production. Herein, the catalytic contribution of Pd–MNPs to lower the overpotential of HER produced at 3D-nCEs was explored in a 0.5 M H_2SO_4 electrolyte by means of linear sweep voltammetry (LSV). The resulting HER LSV curves are illustrated in **Figure 6a**. A notable overpotential decrease from –1.08 V to –0.55 V (*vs.* HRE) was observed at a current density of 10 $mA \cdot cm^{-2}$ once 3D-nCEs were functionalized with Pd–MNPs. Such decrease in the HER overpotential when compared with the unmodified 3D-nCEs means that the hybrid Pd–MNPs@3D-nCE needs much less energy to produce H_2 (≈ 50% as shown in **Figure 6a**, inset). This must be ascribed to the high current density and excellent activity of Pd–MNPs. Therefore, the covalent immobilization of Pd–MNPs is a facile strategy to improve the electrochemical performance of 3D-nCEs for energy conversion purposes.

Additionally, the feasibility of integrating Cu–MNPs upon 3D-nCEs as pathway to accelerate the fast diffusion of electrons for 3D-printed supercapacitors (energy storage) was also explored. **Figure 6b** depicts the cyclic voltammograms achieved in 2 M H_2SO_4

electrolyte. A remarkable capacitance increases of 76 % was achieved (from 870 µF to 1565 µF) when Cu–MNPs were added to the 3D-nCEs, yielding to an areal capacitance value as good as 5.43 mF·cm^{-2} for the Cu@3D-nCE. This higher capacitance value can be ascribed to the increase of the surface area and the redox activity of the electrodes through the incorporation of the Cu–MNPs. Interestingly, this enhanced capacitive response was also maintained over different scan rates, which enabled the Cu@3D-nCE to exhibit an improvement of the rate capability in comparison with the bare electrodes, most likely due to the higher conductivity provided by the Cu-MNPs. Thus, the strategic integration of Cu–MNPs upon carbon-based 3D-printed electronic devices allows supercapacitors with superior electrochemical performances.

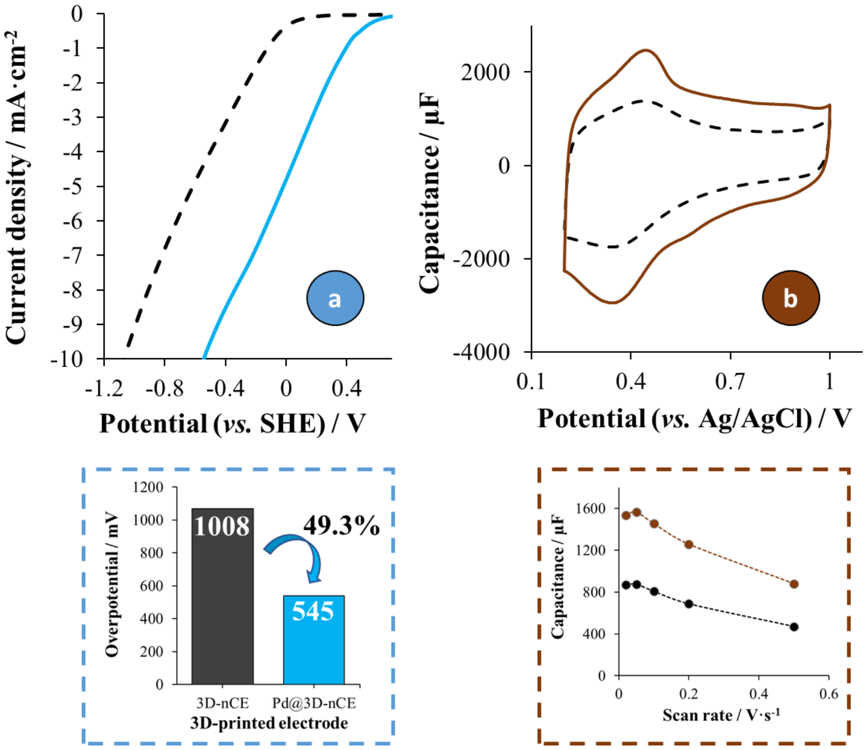

Figure 6. Electrochemical achievements of organic–inorganic 3D-printed electronic interfaces in energy storage & conversion. a) Lineal sweep voltammograms of the HER (electrolyte: 0.5 M H_2SO_4; scan rate: 5 mV·s^{-1}) at the bare (dash line) and Pd-functionalized (solid line) 3D-nCEs. Inset: their corresponding HER overpotential values at -10 mA·cm^{-2}. b) Cyclic voltammograms run in 2 M H_2SO_4 (scan rate: 20 mV·s^{-1}) exhibiting the capacitive current contributions of the bare (dash line) and Cu-functionalized (solid line) 3D-nCEs. Inset: contributions at different scan rates.

2.2.4. Photoelectrochemistry

Since photoelectrochemistry refers to the photon-electricity conversion provided by the electron excitation and following charge transfer of a photoactive material under irradiation,[53] the characteristics of CdS–QDs as photoactive semiconductors were also explored. Chronoamperometry measurements depicted at **Figure 7** shows the photoelectrochemical performance of the developed CdS@3D-nCEs upon switching on and off the irradiation light (λ: 660 nm). Comparing to the bare 3D-nCE (see **Figure 7**, inset), a clear electrochemical improvement (88%) by means of photocurrent intensity was yielded after its functionalization with CdS–QDs. These results demonstrate the suitability of carbon-based 3D-printed substrates to transport the photo-excited electrons from the CdS–QDs and convert them into a readable electrical signal. Additionally, a reproducible photocurrent response was observed after several illumination cycles (ON/OFF), suggesting the potential of CdS@3D-nCEs as switchable 3D-printed optoelectronic devices.

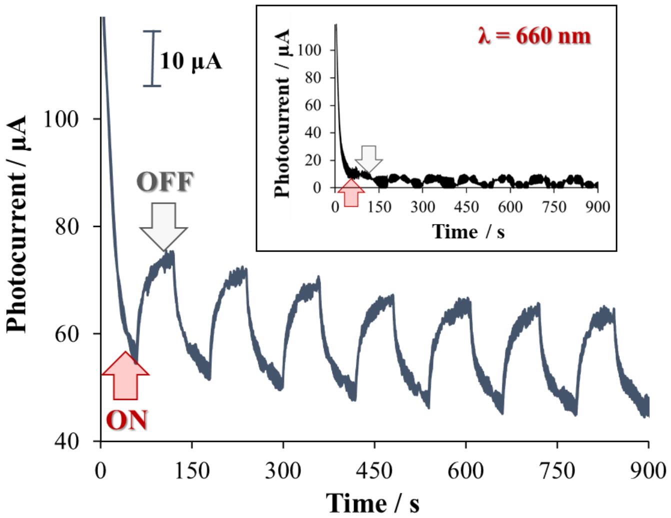

Figure 7. Photoelectrochemical capabilities of organic–inorganic 3D-printed electronic interfaces. Time-based photocurrent response of CdS@3D-nCE and bare 3D-nCE as control (inset) with light ON/OFF. Photoelectrochemical conditions: electrolyte: 0.1 M KCl; bias potential: 0.8 V; illumination source: λ = 660 nm with light intensity ≈100 mW·cm^{-2}.

3. Conclusions

Carbon-based 3D-printed electronic devices have been successfully functionalized with a battery of FINPs *via* fundamental chemistry. The carbon reactivity of 3D-nCE substrates has been exploited for the *in situ* crystallization of metal nanoparticles and quantum dots, resulting in robust functional organic–inorganic 3D-printed electronic interfaces. As a proof-of-concept, the synergism of combining the electronic/optical properties of FINPs with the excellent transducing capabilities of 3D-nCEs has been demonstrated in several areas of electrochemistry (*i.e.*, electrocatalysis, bio-electroanalysis, energy and photoelectrochemistry), resulting in organic–inorganic 3D-printed electronic devices with superior electrochemical performances owing to the implanted catalytic nature of the different FINPs.

Overall, IMS has demonstrated to be a suitable functionalization technique for the custom development of advanced 3D-printed electronic devices acting as catalytic systems by simply transferring the intrinsic properties of FINPs to the 3D-printed transducing platform. Therefore, FINPs have much to offer in the field of 3D-printed electronic devices. In addition, the fused deposition modeling method employed for electrochemical transducers fabrication is general and would allow the exploitation of alternative commercially available conducting filaments, with the benefits of 3D printing technology by means of rapid free-form design and large-scale manufacturing of low-cost electrode architectures. Accordingly, this work paves the way towards the eco-friendly design of the next generation of functional organic–inorganic 3D-printed (opto)electronic devices.

Acknowledgements

J.M. and E. R. contributed equally to this work. M.P. acknowledge the financial support of the Grant Agency of the Czech Republic by the GACR EXPRO 19-26896X project. Authors acknowledge CzechNanoLab Research Infrastructure supported by LM2018110 MEYS CR 2020–2022.

CRediT authorship contribution statement

Jose Muñoz: Conceptualization, Investigation, Formal analysis, Validation, Writing - original draft, Writing - re-view&editing. **Edurne Redondo:** Conceptualization, Investigation, Writing - original draft, Writing – re-view&editing. **Martin Pumera:** Conceptualization, Writing - re-view&editing, Supervision, Funding acquisition.

Declaration of competing interest

The authors declare that they have no known competing financial interests or personal relationships that could have appeared to influence the work reported in this paper.

References

[1] R. Pardo, M. Zayat, D. Levy, *Chem. Soc. Rev.* **2011**, *40*, 672.

[2] Y. Gao, E. Shi, S. Deng, S. B. Shiring, J. M. Snaider, C. Liang, B. Yuan, R. Song, S. M. Janke, A. Liebman-Peláez, P. Yoo, M. Zeller, B. W. Boudouris, P. Liao, C. Zhu, V. Blum, Y. Yu, B. M. Savoie, L. Huang, L. Dou, *Nat. Chem.* **2019**, *11*, 1151.

[3] M. Faustini, L. Nicole, E. Ruiz-Hitzky, C. Sanchez, *Adv. Funct. Mater.* **2018**, *28*, 1704158.

[4] S. H. Mir, L. A. Nagahara, T. Thundat, P. Mokarian-Tabari, H. Furukawa, A. Khosla, *J. Electrochem. Soc.* **2018**, *165*, B3137.

[5] D. Eder, R. Schlögl, *Nanocarbon-Inorganic Hybrids: Next Generation Composites for Sustainable Energy Applications*, Walter De Gruyter GmbH, **2014**.

[6] C. Rogers, W. S. Perkins, G. Veber, T. E. Williams, R. R. Cloke, F. R. Fischer, *J. Am. Chem. Soc.* **2017**, *139*, 4052.

[7] E. Ercan, J. Y. Chen, P. C. Tsai, J. Y. Lam, S. C. W. Huang, C. C. Chueh, W. C. Chen, *Adv. Electron. Mater.* **2017**, *3*, 1700344.

[8] S. H. Baek, J. Roh, C. Y. Park, M. W. Kim, R. Shi, S. K. Kailasa, T. J. Park, *Mater. Sci. Eng. C* **2020**, *107*, 110273.

[9] J. Muñoz, F. Leonardi, T. Özmen, M. Riba-Moliner, A. González-Campo, M. Mas-Torrent, M. Baeza, M. Mas-Torrent, *J. Mater. Chem. C* **2019**, *7*, 14993.

[10] J. Muñoz, R. Montes, J. Bastos-Arrieta, M. Guardingo, F. Busqué, D. Ruíz-Molina, C. Palet, J. García-Orellana, M. Baeza, *Sensors Actuators, B Chem.* **2018**, *273*, 1807.

[11] J. Muñoz, M. Baeza, *Electroanalysis* **2017**, *29*, 1660.

[12] A. N. Shipway, E. Katz, I. Willner, *Nanoparticle Arrays on Surfaces for Electronic, Optical, and Sensor Applications of Our Studies on Nanoparticle Arrays Are Supported by the Israel-U.S. Binational Science Foundation and the German-Israeli Program (DIP).*, WILEY, **2000**.

[13] E. Katz, I. Willner, J. Wang, *Electroanalysis* **2004**, *16*, 19.

[14] W. Yang, J. Zhao, H. Tian, L. Wang, X. Wang, S. Ye, J. Liu, J. Huang, *Small* **2020**, *16*, 2002236.

[15] M. Xia, J. Luo, C. Chen, H. Liu, J. Tang, *Adv. Opt. Mater.* **2019**, *7*, 1900851.

[16] Z. Y. Zhou, N. Tian, J. T. Li, I. Broadwell, S. G. Sun, *Chem. Soc. Rev.* **2011**, *40*, 4167.

[17] P. G. Jamkhande, N. W. Ghule, A. H. Bamer, M. G. Kalaskar, *J. Drug Deliv. Sci. Technol.* **2019**, *53*, 101174.

[18] R. N. Maronesi, D. L. Ferreira, M. L. Lana, M. S. Couto, S. O. Ferreira, A. G. Silva, *J. Lumin.* **2018**, *202*, 489.

[19] J. Bastos-Arrieta, J. Muñoz, A. Stenbock-Fermor, M. Muñoz, D. N. Muraviev, F. Céspedes, L. A. Tsarkova, M. Baeza, *Appl. Surf. Sci.* **2016**, *368*, 417.

[20] J. Muñoz, J. Bastos-Arrieta, M. Muñoz, D. Muraviev, F. Céspedes, M. Baeza, *RSC Adv.* **2014**, *4*, 44517.

[21] A. Kumar, *Manuf. Lett.* **2018**, *15*, 122.

[22] M. P. Browne, E. Redondo, M. Pumera, *Chem. Rev.* **2020**, *120*, 2783.

[23] H. Yang, W. R. Leow, X. Chen, *Small Methods* **2018**, *2*, 1700259.

[24] R. Hensleigh, H. Cui, Z. Xu, J. Massman, D. Yao, J. Berrigan, X. Zheng, *Nat.*

Electron. **2020**, *3,* 216.

[25] V. Urbanová, M. Pumera, *Appl. Mater. Today* **2020**, *21*, 100881.

[26] J. Muñoz, M. Pumera, *ChemElectroChem* **2020**, *7*, 3404.

[27] K. Gnanasekaran, T. Heijmans, S. van Bennekom, H. Woldhuis, S. Wijnia, G. de With, H. Friedrich, *Appl. Mater. Today* **2017**, *9*, 21.

[28] J. Muñoz, E. Redondo, M. Pumera, *Adv. Funct. Mater.* **2021**, *31*, 2010608.

[29] A. Abdalla, B. A. Patel, *Curr. Opin. Electrochem.* **2020**, *20*, 78.

[30] G. Martins, J. L. Gogola, L. H. Budni, B. C. Janegitz, L. H. Marcolino-Junior, M. F. Bergamini, *Anal. Chim. Acta* **2021**, *1147*, 30.

[31] J. Muñoz, M. Pumera, *TrAC Trends Anal. Chem.* **2020**, *128*, 115933.

[32] C. W. Foster, M. P. Down, Y. Zhang, X. Ji, S. J. Rowley-Neale, G. C. Smith, P. J. Kelly, C. E. Banks, *Sci. Rep.* **2017**, *7*, 1.

[33] S. Ng, C. Iffelsberger, J. Michalička, M. Pumera, *ACS Nano* **2021**, *15*, 686.

[34] C. Iffelsberger, S. Ng, M. Pumera, *Appl. Mater. Today* **2020**, *20*, 100654.

[35] K. Fu, Y. Yao, J. Dai, L. Hu, *Adv. Mater.* **2017**, *29*, 1603486.

[36] J. Muñoz, E. Redondo, M. Pumera, *ACS Appl. Mater. Interfaces* **2021**, *13*, 12649.

[37] M. P. Browne, V. Urbanova, J. Plutnar, F. Novotný, M. Pumera, *J. Mater. Chem. A* **2020**, *8*, 1120.

[38] K. Ghosh, S. Ng, C. Iffelsberger, M. Pumera, *Chem. - A Eur. J.* **2020**, *26*, 15746.

[39] M. P. Browne, F. Novotný, Z. Sofer, M. Pumera, *ACS Appl. Mater. Interfaces* **2018**, *10*, 40294.

[40] C. L. M. Palenzuela, F. Novotný, P. Krupička, Z. Sofer, M. Pumera, *Anal. Chem.* **2018**, *90*, 5753.

[41] P. Mondal, A. Sinha, N. Salam, A. S. Roy, N. R. Jana, S. M. Islam, *RSC Adv.* **2013**, *3*, 5615.

[42] D. L. Silva, J. L. E. Campos, T. F. D. Fernandes, J. N. Rocha, L. R. P. Machado, E. M. Soares, D. R. Miquita, H. Miranda, C. Rabelo, O. P. Vilela Neto, A. Jorio, L. G. Cançado, *Carbon N. Y.* **2020**, *161*, 181.

[43] V. A. O. P. Silva, W. S. Fernandes-Junior, D. P. Rocha, J. S. Stefano, R. A. A. Munoz, J. A. Bonacin, B. C. Janegitz, *Biosens. Bioelectron.* **2020**, *170*, 112684.

[44] E. Redondo, J. Muñoz, M. Pumera, *Carbon N. Y.* **2021**, *175*, 413.

[45] P. Zhou, Y. Xie, J. Fang, Y. Ling, C. Yu, X. Liu, Y. Dai, Y. Qin, D. Zhou, *Chemosphere* **2017**, *178*, 1.

[46] C. Gao, F. Lyu, Y. Yin, *Chem. Rev.* **2020**, *121*, 834.

[47] Z. Bai, G. Li, J. Liang, J. Su, Y. Zhang, H. Chen, Y. Huang, W. Sui, Y. Zhao, *Biosens. Bioelectron.* **2016**, *82*, 185.

[48] R. Serra-Maia, M. Bellier, S. Chastka, K. Tranhuu, A. Subowo, J. D. Rimstidt, P. M. Usov, A. J. Morris, F. M. Michel, *ACS Appl. Mater. Interfaces* **2018**, *10*, 21224.

[49] X. Ren, X. Meng, D. Chen, F. Tang, J. Jiao, *Biosens. Bioelectron.* **2005**, *21*, 433.

[50] C. Chen, X. Chang, H. Teymourian, D. E. Ramírez-Herrera, B. Esteban-Fernández de Ávila, X. Lu, J. Li, S. He, C. Fang, Y. Liang, F. Mou, J. Guan, J. Wang, *Angew. Chemie - Int. Ed.* **2018**, *57*, 241.

[51] M. S. Inkpen, Z. –F Liu, H. Li, L. M. Campos, J. B. Neaton, L. Venkataraman, *Nat. Chem.* **2019**, *11*, 351.

[52] J. Muñoz, A. González-Campo, M. Riba-Moliner, M. Baeza, M. Mas-Torrent, *Biosens. Bioelectron.* **2018**, *105*, 95.

[53] M. J. Li, Y. N. Zheng, W. Bin Liang, R. Yuan, Y. Q. Chai, *ACS Appl. Mater. Interfaces* **2017**, *9*, 42111.